Journal of African Earth Sciences 196 (2022) 104729

Contents lists available at ScienceDirect

Journal of African Earth Sciences

journal homepage: www.elsevier.com/locate/jafrearsci

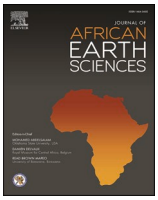

Fault plane picking from focal mechanisms in reverse faulting stress: Application to the Mw6.9 Boumerdes (Algeria) earthquake sequence

Reda Ouyed [a,*], Mohamed Salah Boughacha [a], Mourad Bezzeghoud [b], Václav Vavryčuk [c,d]

[a] Laboratoire de Géophysique, Faculté des Sciences de la Terre, de la Géographie et de l'Aménagement du Territoire, Université des Sciences et de la Technologie Houari Boumediene (USTHB), Algiers, Algeria
[b] Departamento de Física and Centro de Geofísica Évora, Instituto de Ciências da Terra, Universidade de Évora, Évora, Portugal
[c] Institute of Geophysics, Czech Academy of Sciences, Prague, Czech Republic
[d] Institute of Geology, Czech Academy of Sciences, Prague, Czech Republic

ARTICLE INFO

Keywords:
Focal mechanisms
Fault identification
Fault instability method
Slip angle criterion

ABSTRACT

Identification of the fault plane from two nodal planes of the focal mechanism is, in general, ambiguous. This problem is commonly solved using other constraints provided by tectonic, geological or seismic studies. In this paper, we evaluate the probability of identifying the fault plane using knowledge of stress field. We employ two alternative methods: (1) the slip angle method (SA), and (2) the highest instability method (IS). First, the efficiency of the methods was tested on synthetic data consisting of focal mechanisms compatible with a reverse stress regime. The tests revealed that the fraction of faults correctly picked by the IS method is higher than that of the SA method, particularly for large noise values. Second, the methods were applied to the aftershocks of the Boumerdes (Algeria) earthquake of May 21, 2003. This application showed that when taking into account the focal solutions for which the fault planes are determined using the IS method with a high probability, we observe consistency between the selected faults and the tectonics of the study area.

1. Introduction

Knowledge of tectonic stress is essential for understanding tectonics and behaviour of faults in seismically active regions. Several computational methods for determining the stress from fault parameters have been developed. Bott (1959) studied the direct problem and Arthaud (1969) developed a graphical method in the case of a uniaxial stress. Carey and Brunier (1974) were the first to publish the results of a practical test for the determination of the stress tensor from two fault populations in the Paphos (Cyprus) and Morvan (France) regions. Carey (1976) used an inverse method by minimizing the angular deviation between the observed and calculated striae. Subsequently, Angelier (1979, 1984) and Angelier et al. (1982) proposed several non-linear inversions, while the first linear inversion was introduced by Michael (1984, 1987).

Most of the stress inversion methods (Angelier, 1979; Armijo et al., 1982; Gephart and Forsyth, 1984; Michael, 1984, 1987) are based on the following two assumptions:

i) The stress state is uniform throughout the study area. It is therefore considered that all the faults used for the inversion were activated by the same stress tensor.
ii) The tangential stress acting on the fault plane is parallel to the slip vector. This is known as the Wallace-Bott criterion (Wallace, 1951; Bott, 1959), which can be written as follows:

$$\frac{\vec{\tau}}{|\vec{\tau}|} = \frac{\vec{s}}{|\vec{s}|}, \tag{1}$$

where $\vec{\tau}$ is the tangential stress on the fault plane and $\vec{s}$ the slip vector.

If these two assumptions are satisfied and we know orientations of a fault and slip along the fault for a set of earthquakes, the method allows determining four parameters of the stress tensor: the three directions of the principal stresses σ_1, σ_2, and σ_3 and the shape (stress) ratio

$$R = \frac{\sigma_1 - \sigma_2}{\sigma_1 - \sigma_3}, \tag{2}$$

The stress inversion method can be directly applied, for example, to the slickenside data, which provide the strike and dip of the fault planes,

* Corresponding author.
E-mail address: rouyed@usthb.dz (R. Ouyed).

https://doi.org/10.1016/j.jafrearsci.2022.104729
Received 9 February 2022; Received in revised form 12 September 2022; Accepted 12 September 2022
Available online 20 September 2022

in addition to the rake angle that defines the slip along the fault. In seismology, the problem is, however, more complicated. We usually determine focal mechanisms from seismic records represented by two nodal planes, but we do not know in many cases, which nodal plane is the fault and which nodal plane is the auxiliary plane defining the slip direction. This ambiguity can be removed by geological or seismological considerations, which are not always available.

In order to solve the ambiguity problem, several authors proposed stress inversion methods capable to pick the fault plane during the inversion process. For example, Gephart and Forsyth (1984) developed an inversion method based on a grid search technique when both alternatives of the fault orientations are considered and compared to find which of them yields better fit between the shear stress and the slip direction. Lund and Slunga (1999) suggested two criteria for selecting the actual fault plane. The first one is based on the slip angle method (SA) which picks the plane of the lowest misfit. The second one is the instability method (IS) that selects the nodal plane with the highest instability.

In the present paper, we first established the expression of the instability coefficient that is used in our calculations, and then compared the two fault plane selection criteria IS and SA through the forward problem using synthetic data. In our application, we followed the approach of Vavryčuk (2011, 2014), who incorporated the instability method of Lund and Slunga (1999) into the stress inversion developed by Michael (1984, 1987). This method is applied to focal mechanisms of aftershocks of the May 21, 2003 Boumerdes earthquake.

2. Fault-plane identification

Focal mechanism consists of two nodal planes perpendicular to each other; one of them is the fault while the other is the auxiliary plane. For a successful stress inversion, it is necessary to decide which of the two nodal planes is the fault. If the auxiliary and the fault planes are swapped, the results can be inaccurate and biased particularly for the shape ratio, as it has been emphasised by Vavryčuk (2014). Recent studies (Vavryčuk, 2014, 2015; Martínez-Garzón et al., 2016) investigated the stress inversion accuracy for focal mechanisms through the rotation angle between imposed and retrieved stress axes and the uncertainties of the shape ratio R. This accuracy has been computed for differently accurate focal mechanisms. Computations were performed on synthetic tests using one uniform stress tensor and a shape ratio of 0.7 for Vavryčuk (2014) and the three Andersonian regimes (reverse, strike-slip and normal faulting) with $R = 0.1$, 0.5 and 0.9 for Martínez-Garzón et al. (2016). It has been shown that the principal stress axes were determined with similar accuracy for the original Michael's inversion method as well as for the inversion based on the slip angle misfit or the instability criterion. However, the instability criterion method allowed having more reliable R values.

In this section, we deal with theoretical aspects of the problem, whereas, synthetic tests will be presented in the next section.

2.1. Mathematical description of stress

We consider stress tensor in the coordinate system defined by principal stress axes:

$$\boldsymbol{\sigma} = \begin{bmatrix} \sigma_1 & 0 & 0 \\ 0 & \sigma_2 & 0 \\ 0 & 0 & \sigma_3 \end{bmatrix}, \tag{3}$$

where σ_1, σ_2 and σ_3 are called the maximum, intermediate and minimum principal stresses (compression is positive).

The stress vector $\vec{T}(T_1, T_2, T_3)$ acting on a plane oriented by its normal $\vec{n}(n_1, n_2, n_3)$ can be expressed as:

$$T_i = n_j \sigma_{ij}\,, \tag{4}$$

with its normal and shear components $\vec{\sigma_n}$ and $\vec{S}$

$$\vec{\sigma_n} = \left(\vec{n} \cdot \vec{T}\right)\vec{n}\,, \tag{5}$$

and

$$\vec{S} = \vec{T} - \vec{\sigma_n}. \tag{6}$$

We can extract the shear stress components $\vec{S}(S_1, S_2, S_3)$ acting on the plane from eq. (6), and write the shear stress magnitude $\left|\vec{S}\right|$ and the slip vector $\vec{S}$ into the form given by Lund and Slunga (1999) and Armijo et al. (1982):

$$\left|\vec{S}\right| = (\sigma_1 - \sigma_3)\sqrt{n_3^2 + R^2 n_2^2 - K^2}\,, \tag{7}$$

$$\vec{S} = \frac{1}{\sqrt{n_3^2 + R^2\, n_2^2 - K^2}} \begin{bmatrix} K\, n_1 \\ (K - R)\, n_2 \\ (K - 1)\, n_3 \end{bmatrix}. \tag{8}$$

with $K = n_3^2 + R\, n_2^2$. (9)

Eq. (8) shows that the direction of the shear stress depends only on the shape ratio R and the orientation of the plane described by its normal $\vec{n}$. We can therefore compute the slip vector $\vec{s}$ by geometrical considerations from the earthquake focal mechanisms. However, eq. (7) shows that the magnitude of the tangential stress depends on magnitude of principal stresses. This property has been underlined by Bott (1959) and Armijo et al. (1982). The above expressions will help to establish the instability coefficient.

2.2. Instability coefficient determination

As stated earlier, the problem with ambiguous fault plane orientations in stress inversions can be solved by slip angle (SA) or instability (IS) methods. The first one proposed by Gephart and Forsyth (1984) is based on minimizing the deviation between the direction of the shear stress and the slip vector along the fault. The nodal plane with the minimal deviation is considered to be the fault plane. By contrast, the IS method selects the plane with the highest instability that could be defined over the Mohr-Coulomb failure criterion (Jaeger et al., 2007) (compression is positive)

$$\tau_c = S_0 + \mu\sigma \tag{10}$$

or

$$\tau_c = S_0 + \mu(\sigma_n - p)\,, \tag{11}$$

where τ_c is the critical shear stress, S_0 denotes the cohesion and μ the fault friction usually ranging between 0.6 and 0.8 (Byerlee, 1978). Quantities σ, σ_n and p are the normal effective stress, the normal stress and pore pressure, respectively. If the shear stress acting on a fault plane exceeds the critical value (τ_c), then the fault becomes unstable and an earthquake can occur (Vavryčuk, 2015). Fig. 1 follows the scheme proposed by Vavryčuk (2015) and shows the necessary elements for computing the instability coefficient I.

From triangle APD, where the coordinates of point P are (σ_1,0), it follows that:

$$\mu = \tan\varphi, \tag{12}$$

$$\overline{PD} = \overline{AP}\sin\varphi. \tag{13}$$

Knowing that

$$\sin\varphi = \frac{\mu}{\sqrt{1 + \mu^2}}, \tag{14}$$

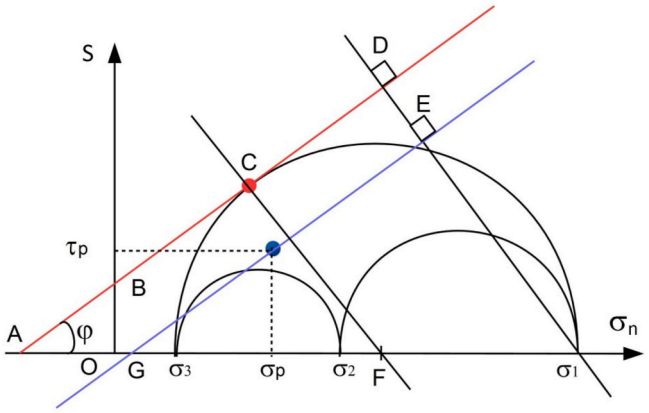

Fig. 1. Mohr's circle diagram which describes the changes of shear stress S as a function of normal stress σ_n. Symbols σ_1, σ_2 and σ_3 are the most, intermediate and least compressive principal stresses, respectively. The red line which is tangent to the Mohr's circle (point C) and corresponds to the most unstable plane ($I = 1$) is parallel to the Coulomb failure criterion line. The red line is also parallel to the blue one passing through the blue point corresponding to a plane on which the shear and normal stresses are τ_p and σ_p, respectively.

it is enough to compute

$$\overline{AP} = \overline{AO} + \sigma_1. \tag{15}$$

From triangle AFC, we have the expression for $\overline{AO}$:

$$\overline{AO} = \frac{\sigma_1 - \sigma_3}{2}\ \frac{\sqrt{1+\mu^2}}{\mu}\ \frac{\sigma_1 + \sigma_3}{2}. \tag{16}$$

From eqs (13), (15) and (16) we obtain the expression for $\overline{PD}$:

$$\overline{PD} = \frac{\sigma_1 - \sigma_3}{2}\left(1 + \frac{\mu}{\sqrt{1+\mu^2}}\right). \tag{17}$$

We can observe that $\overline{PD}$ which relates to the most unstable fault is a function of the coefficient of friction μ and the differential stress $(\sigma_1 - \sigma_3)$.

In order to evaluate the instability of a fault plane defined by its normal $\vec{n}(n_1, n_2, n_3)$ in the principal coordinate system, we need the magnitude of $\overline{PD}$. Based on the definition of the fault instability coefficient I given by (Vavryčuk et al., 2013), we can write:

$$I = \frac{\overline{PE}}{\overline{PD}} \tag{18}$$

As a result, the planes corresponding to the blue line in the Mohr diagram (Fig. 1) have the same instability factor I.

$\overline{PE}$ can be expressed from Fig. 1 and eq. (14) as

$$\overline{PE} = \overline{GP}\sin\varphi = \overline{GP}\frac{\mu}{\sqrt{1+\mu^2}}. \tag{19}$$

$$\text{Knowing that : } \overline{GP} = \overline{GH} + \overline{HP} = \frac{\tau_p}{\mu} + (\sigma_1 - \sigma_p)\ , \tag{20}$$

where σ_p is the normal stress magnitude related to the fault plane oriented by its normal $\vec{n}$ and τ_p the corresponding shear stress. These two variables can be derived from eqs. (5) and (7), respectively.

We have

$$\overline{PE} = \frac{\mu(\sigma_1 - \sigma_3)}{\sqrt{1+\mu^2}}\left(\frac{\sqrt{n_3^2 + R^2 n_2^2 - K^2}}{\mu} + n_2^2 R + n_3^2\right) \tag{21}$$

we find the expression of the instability coefficient I:

$$I = \frac{\overline{PE}}{\overline{PD}} = \frac{2}{\mu + \sqrt{1+\mu^2}}\left(\sqrt{n_3^2 + R^2 n_2^2 - K^2} + \mu\left(n_2^2 R + n_3^2\right)\right) \tag{22}$$

It is noteworthy that I is independent of the stress magnitude. It depends only on the components of the normal to the fault plane (n_1, n_2, n_3), friction coefficient μ and shape ratio R.

We have validated our results by comparing them with those obtained from Vavryčuk formula (2013, 2014, 2015). It is important to point out that, on the opposite to Vavryčuk et al. (2013), we made no assumption about scaling of the reduced stress. Furthermore, we can observe that our expression of the fault instability coefficient is simpler than that of Vavryčuk et al. (2013).

3. Synthetic tests

In this section, we compute the probability of identifying the correct fault plane according to the SA and IS criteria using synthetic data. These computations are performed for reverse faulting that corresponds to the stress regime acting in the region under study. This stress regime is represented by uniform stress field where the most and least compressive principal stresses are oriented in NS and vertically, respectively (Anderson, 1951). Under the above mentioned conditions and for a given stress ratio R, we create 1000 synthetic focal mechanisms by randomly sampling the strike and dip angles and selecting the fault plane satisfying the Mohr-Coulomb failure condition. The chosen number of focal mechanisms provides quite stable results. The corresponding rake angles are computed according to the Wallace-Bott criterion (Wallace, 1951; Bott, 1959). Uniform random noise has been added independently to the three geometrical parameters of the fault (strike, dip and rake) with a value up to threshold levels from 5° to 40°. This approach has already been used by Vavryčuk (2015) and Martínez-Garzón et al. (2016). Fig. 2 depicts a sample of 50 noise-free synthetic focal mechanisms (beach balls) with the corresponding Mohr representation (inset), in agreement with the reverse faulting stress regime.

A similar work was carried out by Gephart and Forsyth (1984) who suggested that a pick is considered correct if the misfit is less than 20° and the difference between the misfits of the fault and the auxiliary planes is greater than 10°. As suggested by Michael (1987), if we apply a stringent criterion, the picks would be substantially correct, but we get a low number of picks. Following this idea, we propose to investigate the rates of success in picking the correct fault planes in relation with: (i) the

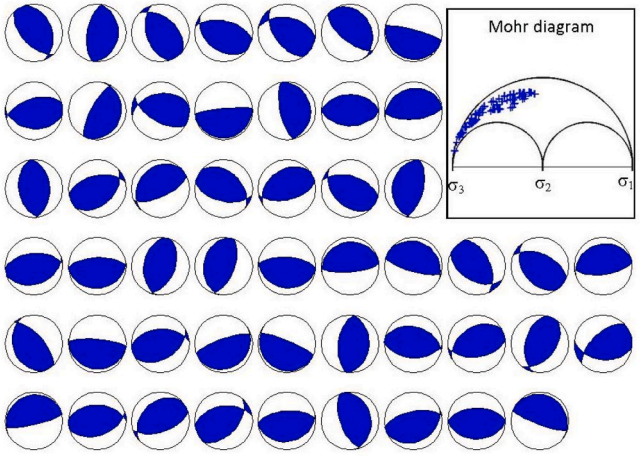

Fig. 2. Sample of 50 synthetic focal mechanisms generated in the case of reverse faulting regime with the most compressive stress σ_1 oriented in NS and the vertical least compressive stress σ_3 (Anderson, 1951). Noise-free, friction coefficient $\mu = 0.5$ and shape ratio $R = 0.5$. Inset: Mohr's circle diagram with positions of faults (plus signs).

maximum misfit in combination with the minimum misfit difference (minimum Δm) and (ii) the minimum instability in combination with the minimum instability difference (minimum ΔI). Expressed otherwise, it is about the probability of determining the correct fault planes with a misfit lower than a predefined value (maximum misfit) and a misfit difference (Δm) higher than a predefined value (minimum misfit difference). The same rule is applied to the case of the instability criterion. This means that the probability of picking the correct fault planes is expressed in terms of instability I higher than a predefined value (minimum instability) and an instability difference (ΔI) higher than a minimum instability difference.

In the first step, we propose to study the relationship between the probability of identifying the fault plane and noise level. Fig. 3 shows the results obtained when the friction coefficient is equal to 0.5 and the shape ratio having values of 0.2, 0.5 and 0.8. We can clearly observe that the robustness of the selection criterion depends not only on friction μ and shape ratio R, but also on the noise level (Fig. 3). If we consider a low R value (0.2) as an example, the instability criterion (blue triangles) gives much better results than the misfit criterion (blue crosses), independently of the noise level. If R is larger (0.8), the instability criterion (red triangles) gives better results for low noise, while the misfit criterion is better for high noise. Of course, the number of correctly picked fault planes decreases as the noise level increases, and we obtain a probability that varies between 55% and 70% for a noise level of 45° and between 80% and 92% for a noise level of 10°.

Fig. 3 shows the complexity of the probability change in identifying fault planes as a function of the shape ratio R, friction μ and noise level. We therefore display in Fig. 4 this variation according to a wider range of these three variables. In order to compare all the achieved results, we have considered in Fig. 4 the same colour scale of the noise level for the two selection criteria. Indeed, the probability of correctly picked faults is given as a function of the shape ratio R (y-axis) and the friction coefficient μ (x-axis) for noise levels of 10°, 20°, 30° and 40° (shown at the right of Fig. 4).

Fig. 4 (left) depicts the fraction of correctly picked faults as a function of friction μ (x-axis) and the shape ratio R (y-axis), when the instability method (IS) is used. It is obvious from this figure that whatever the noise level is, the probability increases with μ, so that the highest probability is observed for large friction values. However, the lowest probability is for large R and low μ values. On the other hand, when the SA criterion is applied (Fig. 4, middle), the highest probability of correctly picked faults is observed for high friction with the shape ratio ranging between 0.5 and 0.7, depending on the noise level, while the lowest probability is for lower and higher R (around 0.1 and 0.8) values. The difference between the probabilities of identified faults for the IS and SA methods (Fig. 4, right) shows that, as a whole, the instability (IS) criterion is more suitable than the slip angle (SA) method to clear up the fault plane ambiguity, particularly for large noise and low R values.

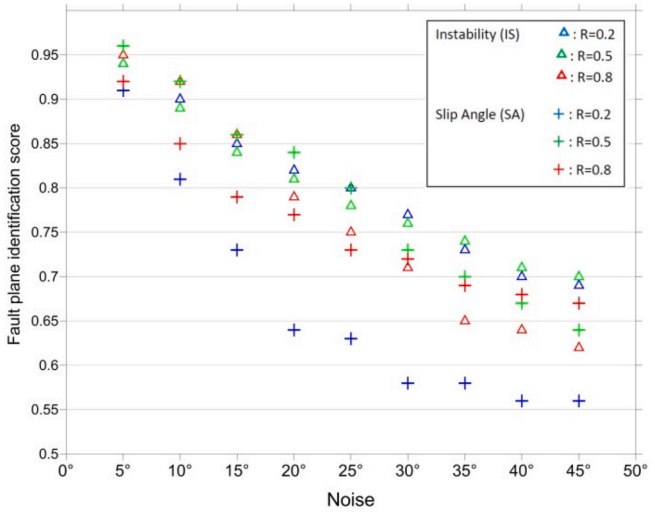

Fig. 3. Fault plane identification score as a function of noise level (5°–45°) for reverse faulting, $\mu = 0.5$ and $R = 0.2$, 0.5 and 0.8. Plus signs and triangles relate to the slip angle (SA) and the fault instability (IS) criteria, respectively.

In this paragraph, we will compare our results with those obtained by Martínez-Garzón et al. (2016) who used the iterative approach of Vavryčuk (2014) to assess the probability of correctly identified faults by applying the SA and IS criteria to synthetic tests. They concluded that the SA criterion fails to pick the correct fault planes in the reverse stress regime regardless of the noise levels, in contrast to the results of the direct problem where the probability of picking correct faults can exceed 70%, even if the noise level is of 40° as for the results shown in Fig. 4 (middle); this is indeed observed for R and μ above 0.5. This is even more evident for the IS criterion. On the other hand, the results that were found by the authors showed that the performance of the IS criterion in picking the correct faults is nearly the same for $R = 0.1$, 0.5 and 0.9 that is inconsistent with the results found by the direct problem (Fig. 4). This feature will be discussed in more detail in Section 5.

The probability of correctly picked fault planes can also be investigated (Fig. 5) for a maximum misfit (as shown on x-axis) and a minimum misfit difference (minimum Δm) between the two nodal planes (as shown on y-axis) in two different ways: (i) with respect to focal mechanisms that meet the requirements of x and y axes (Correctly Picked/Selected, CP/S) (Fig. 5a). (ii) With respect to all focal mechanisms (Correctly Picked/Total, CP/T) (Fig. 5b). Moreover, the fraction of focal mechanisms that meet the conditions of x and y axes with respect to all used focal mechanisms have been computed (Fig. 5c); it is merely the ratio between CP/T and CP/S. Computations are for reverse faulting regime, shape ratio $R = 0.5$, $\mu = 0.5$ and noise level is 30°.

As for the SA method, we also investigated the success of choosing the correct fault plane with the highest instability criterion. Thus, Fig. 5d, e and f depict the probability of picking the fault plane for the instability higher than the 'minimum instability' of the x-axis and the instability difference between the two nodal planes higher than the 'minimum instability difference (minimum ΔI)' represented by the y-axis. In Fig. 5, the same colour scale has been used to display the probability of picking the fault planes. As a consequence, the figures showing CP/S for both fault plane selection criteria have a low resolution (Fig. 5a and d), and hence, cannot be correctly interpreted. We therefore display the results using a reduced colour scale consistent with the obtained values (Fig. 6). As expected, this new representation highlights in a more refined way the increase of the fraction of correctly picked faults with respect to the selected focal mechanisms (CP/S) with the minimum Δm for SA and with the minimum ΔI for IS (Fig. 6).

It is noteworthy that the rates of success in picking the correct fault planes with the SA and IS criteria, depends only on the minimum misfit difference and the minimum instability difference, respectively. Indeed, Figs. 5 and 6 clearly show that the maximum misfit and the minimum instability do not affect the probability of picking the correct fault planes for the SA and IS methods. Under these conditions, it will be necessary to take into account all the misfits, for the SA method, and all the values of the instability when applying the IS criterion. Depending on the method used (SA or IS), the fault plane selection will thus be performed only through the misfit and instability differences between the two nodal planes.

For tectonic analysis and interpretation, it would be useful to evaluate the probability of the used fault planes being correctly picked with a sufficient number. We must therefore compute this probability with respect to the focal mechanisms that meet the minimum Δm (misfit difference) condition (Correctly picked/selected, CP/S) and with respect to all focal mechanisms (Correctly picked/total, CP/T). In this context, we present in Fig. 7 (black circles) the minimum Δm as a function of the CP/S related to the x-axis and the CP/T to the y-axis. The same approach

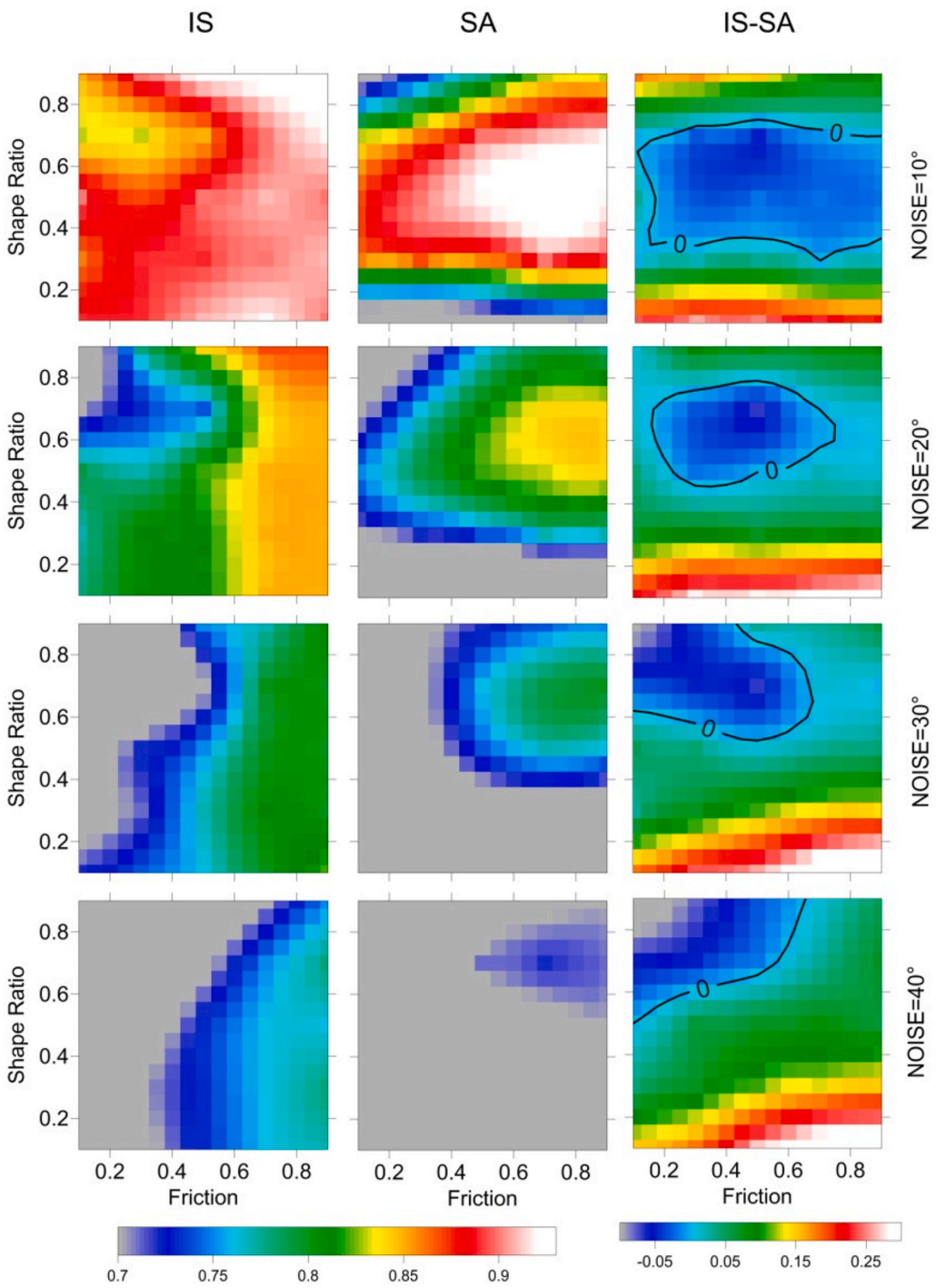

Fig. 4. Fraction of correctly identified faults as a function of shape ratio R and friction μ for the maximum instability IS (left), minimum slip angle (SA) (middle), and the difference between the last two fractions (left – middle) (right). Computations were performed for reverse stress regime and a noise level of 10°, 20°, 30° and 40°, as depicted on the right of the figure.

has been applied for the IS criterion (red circles in Fig. 7). These computations have been performed for noise level of 30°, $\mu = 0.5$, $R = 0.5$ and reverse faulting regime.

As an example, if we use the SA method and intend to represent and interpret the orientations of faults having 85% probability for a nodal plane of being chosen as a fault plane, one might determine from Fig. 7 (black circles) the minimum Δm (20°) and the corresponding total number of correctly picked fault planes (0.45). In other words, for 100 focal mechanisms, we can extract 45 fault planes (CP/T, y-axis of Fig. 7) that represent 85% (CP/S, x-axis of Fig. 7) of those having a misfit difference higher than 20° (black circles of Fig. 7). If this probability increases from 85% to 95%, one can see that the total number of identified faults is only 30 instead of 45 as shown in Fig. 7. This leads to Δm of about 30°. This shows that as the minimum misfit or instability difference between the two nodal planes increases, CP/S increases, but CP/T decreases. If CP/S is taken relatively large, then CP/T would be too small for this interpretation. It is then necessary to maintain a balance between CP/T and CP/S. In this particular case, the IS and SA methods yield almost identical results. However, in a more general way, the IS method picks the correct fault planes more successfully than the SA

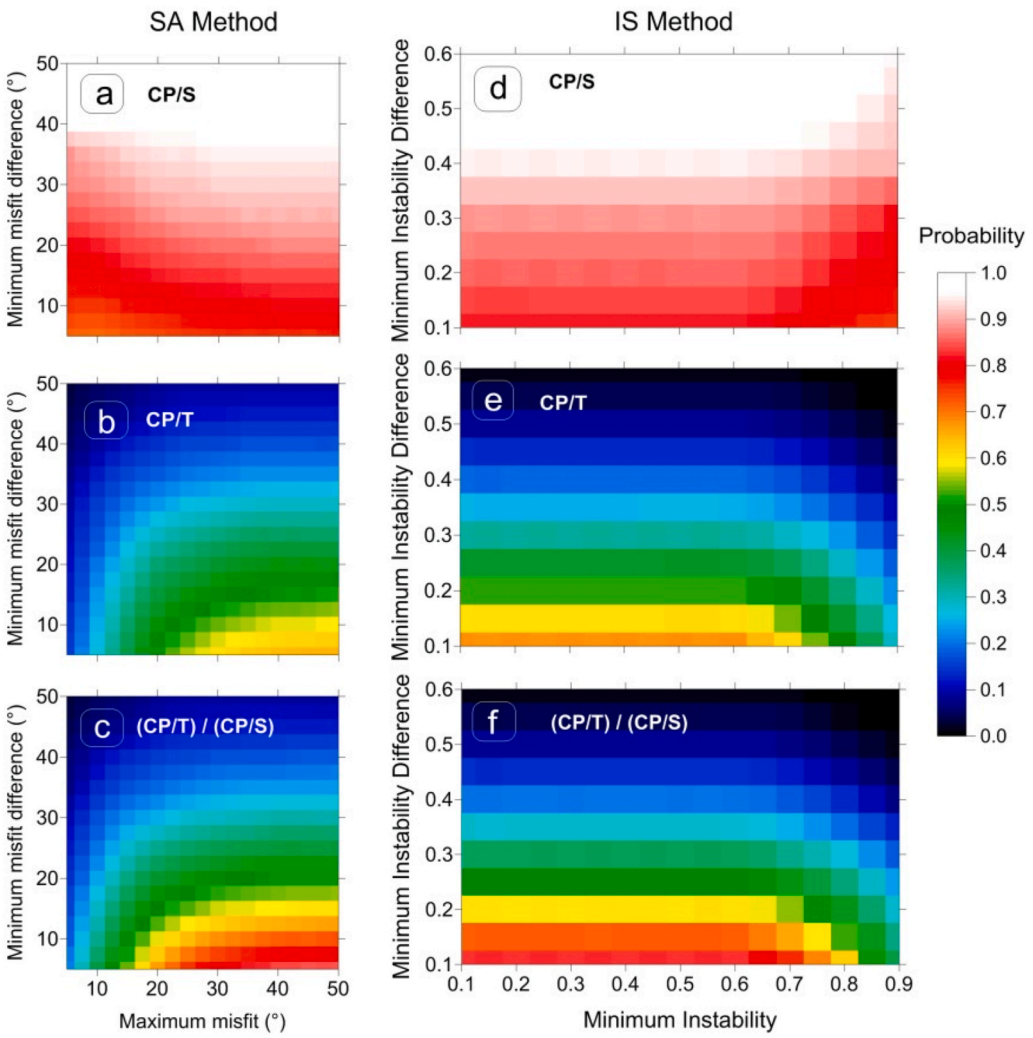

Fig. 5. (a) and (d) Fraction of correctly picked fault planes with respect to the focal mechanisms that meet the requirements of x and y axes (Correctly Picked/Selected, CP/S). (b) and (e) Fraction of correctly picked fault planes that satisfy the conditions stated on the x and y axis, with respect to all the used focal mechanisms (Correctly Picked/Total, CP/T). (c) and (f) Fraction of focal mechanisms that meet the requirements of x and y axes, with respect to all the used focal mechanisms; this amounts to dividing CP/T by CP/S. In the left panel (a, b and c) the x–axis is for misfits lower than the 'maximum misfit' and the y-axis for the misfit difference higher than the 'minimum misfit difference'. In the right panel (d, e and f), the x-axis relates to the instability coefficient higher than the 'minimum instability' and y-axis to the instability difference higher than the 'minimum instability difference'. Computations are for reverse faulting, $R = 0.5$, $\mu = 0.5$ and noise level is 30°.

method, as depicted in Fig. 4 which in fact is related to the CP/T for minimum $\Delta I = 0$ (for IS method) and minimum $\Delta m = 0$ (for SA method).

We also investigated the changes of minimum Δm and minimum ΔI as a function of CP/S and CP/T for different noise levels (Fig. 8). We can point out that, for the SA criterion (Fig. 8a), CP/S is between 0.9 and 1 for a noise level of 20°. If noise level increases by 10°, CP/S probability is being reduced by approximately 0.1 (Fig. 8a), whereas this reduction is lower for the IS criterion (Fig. 8b). In fact, the quantities CP/S and CP/T vary according to several parameters including the shape ratio R, the friction μ and the minimum Δm and ΔI. Hence, it is not possible to illustrate the CP/S and CP/T variations as a function of R and μ as it has been done for the fraction of fault plane identification without any condition on Δm and ΔI (see Fig. 4). Of course, the orientation of the principal stresses must also be taken into account. For the synthetic tests we have considered only the reverse faulting regime. The above mentioned quantities must therefore be estimated in each particular case, as will be done in the next section.

4. Case study: aftershocks sequence of the Boumerdes (Algeria) earthquake of May 21, 2003 ($M_w = 6.8$)

Northern Algeria experienced several moderate to strong earthquakes during the last centuries (Rothé, 1950; Benouar, 2004), in relation with a relatively low rate convergence between the African and Eurasian plates. In this seismotectonic context, a destructive earthquake (Mw = 6.8) hit Boumerdes area on May 21, 2003 (Yelles et al., 2004), where studies conducted by Pelaez-Montilla et al. (2003) and Hamdache et al. (2010) showed that seismic hazard has been fairly low until the occurrence of this seismic event.

GPS measurements and coastal uplift data (Meghraoui et al., 2004) indicated a dislocation model constituted of a SE dipping 50 km long reverse fault striking SW-NE. From teleseismic, GPS and coastal uplift data, Delouis et al. (2004) suggested a similar model, in agreement with the Harvard CMT focal mechanism (Fig. 9). These results were also highlighted by the aftershocks distribution and seismic tomography studies performed by Ayadi et al. (2008) and Kherroubi et al. (2017).

In this section, we applied our method to the focal mechanisms (Fig. 9) computed by Ayadi et al. (2008) and Kherroubi et al. (2017) to assess the probability of correctly picked faults that allows a tectonic interpretation as suggested above. We have made a compilation of 30 focal mechanisms reported by Ayadi et al. (2008, their Table 1) and 82 focal mechanisms reported by Kherroubi et al. (2017, their Table 1), resulting in a total of 104 focal mechanisms of which 8 are the same for the two data sets (Fig. 9). Most of the focal solutions are reverse mechanisms as for the main earthquake, especially around the epicentre and in the eastern part of the study area. However, in the westernmost part, we can observe some strike slip and normal focal solutions.

Using the available focal mechanisms, we computed the stress tensor by applying the STRESSINVERSE code developed by Vavryčuk (2014) for calculating the principal stress directions and the shape ratio R. Subsequently, we evaluated the fault instability I for all nodal planes, and the planes with the highest I (more unstable) were used in the

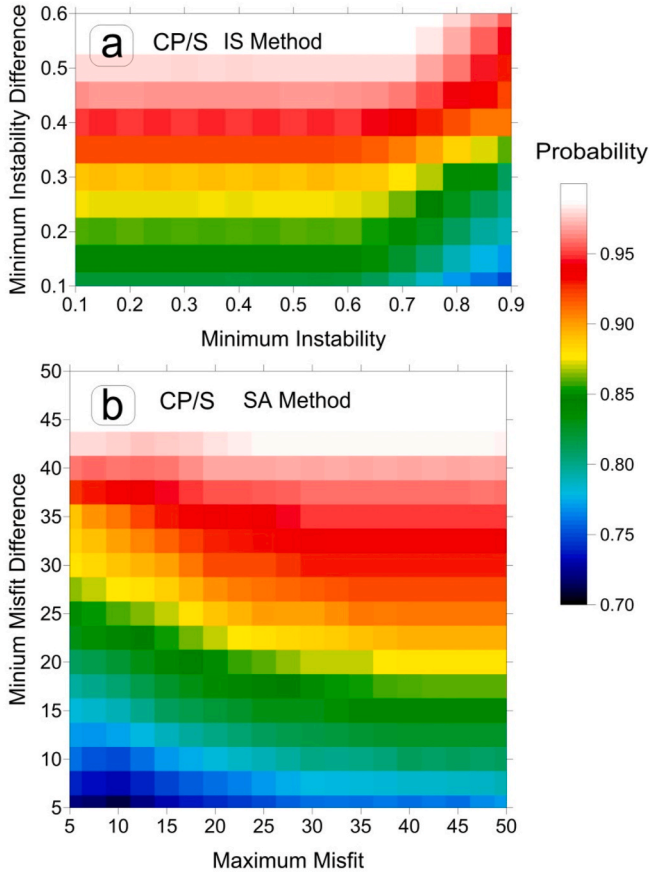

Fig. 6. Fraction of correctly picked fault planes (colour-coded) with respect to focal mechanisms that meet the requirements of x and y axis (CP/S), (a) for the IS and (b) for the SA fault selection methods. Computations are for $R = 0.5$, $\mu = 0.5$, noise level of 30° and reverse faulting regime.

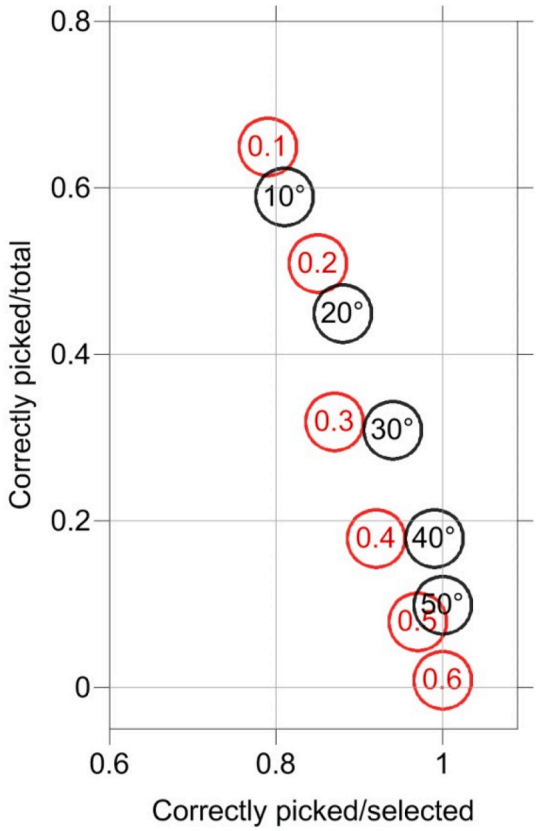

Fig. 7. Values (black circles) of the minimum Δm as a function of correctly picked fault planes with respect to the focal mechanisms that meet the minimum misfit difference (CP/S) (x-axis) and with respect to all the focal mechanisms (CP/T) (y-axis). Values in the red circles are for the minimum ΔI as a function of the same parameters as those used previously. Computations are for noise level of 30°, $\mu = 0.5$, $R = 0.5$ and reverse faulting regime.

successive stress inversion. The iterative process is repeated until it converges to some optimum value. For assessing the instability I, we need to know friction μ, which is evaluated by running the inversion for several values of friction and adopting the value associated with the highest overall instability I (Vavryčuk, 2014).

The application of Vavryčuk's code allows evaluating σ_1, σ_2 and σ_3 principal stress directions (azimuth/plunge), shape ratio R and friction μ: 142°/18°, 50°/8°, 296°/70°, 0.21 and 0.55, respectively. The maximum principal stress σ_1 is nearly horizontal and oriented NW-SE, in agreement with the convergence direction between African and Eurasian plates (Argus et al., 1989; Nocquet and Calais, 2004). The principal stress directions similar to those computed by Kherroubi et al. (2017) being shown in Fig. 10a together with the P and T axes of the focal mechanisms. Fig. 10b shows that the assumed fault planes are concentrated in the upper and lower left parts of the Mohr's circle diagram where slip should occur selectively on fault planes that have relatively high shear stresses and low normal stresses.

Considering the retrieved orientations of the principal stress axes, the shape ratio R and friction coefficient μ, we investigated the probability of correctly picked faults among all the nodal planes of the focal mechanisms. Fig. 11 shows the change of fraction of the identified faults as a function of noise level with respect to all the focal mechanisms for the IS criterion (triangles) and the SA criterion (plus signs). It is noteworthy to mention that the fault identification score is more significant for the instability (IS) criterion than the misfit angle (SA) one (Fig. 11).

Fig. 12 is based on values from Table 1 and it depicts the minimum instability difference as a function of correctly picked faults with respect to the planes that meet the condition of minimum instability difference (CP/S, x-axis) and with respect to all the nodal planes (CP/T, y-axis) for a noise level of 20° (black circles) and 40° (red circles). We have no indication of the accuracy of the focal mechanisms of the Boumerdes earthquake sequence, so it is difficult to assign them the CP/S and CP/T values. If we take an unfavourable case by choosing a noise of 40°, from Table 1 or Fig. 12, we obtain 88% of correctly picked faults among the selected planes (CP/S) and 50% CP/T fraction for a minimum ΔI of 0.40.

When we consider the results of the focal mechanisms inversion obtained from the STRESSINVERSE code (Vavryčuk, 2014), we can observe that out of 104 events, 50 events were found to have ΔI higher than 0.40. Fig. 12 and Table 1 show that 88% of the 50 nodal planes should therefore be faults. It is reasonable to assume that 50 nodal planes with 88% probability of being chosen as fault planes allow a valid tectonic interpretation of the study area. Fig. 13 shows the strikes and dipping directions of the 50 fault planes with their associated instability coefficients.

The seismic events, for which we have associated a fault plane, can be subdivided into three groups. The first one is the cluster located at the SW end of the main fault for which the aftershock fault planes show mainly a high diversity in strike (Figs. 13 and 14a), but more NW-SE oriented faults. The second group, located onshore and east of the first one (Fig. 14b), shows aftershock fault planes dipping SSE to ESE, with strikes consistent with that of the main fault and its dip direction. The third group (Fig. 14c) consists of seismic events located offshore and displays a high diversity in strike (Fig. 13).

We point out that the SW cluster (the first group) would be correlated to the SW part of the main fault model proposed by Bellabès et al. (2009) from a joint inversion of interferometric synthetic aperture radar, coastal uplift, and GPS. Indeed, this is the preferred curved fault model

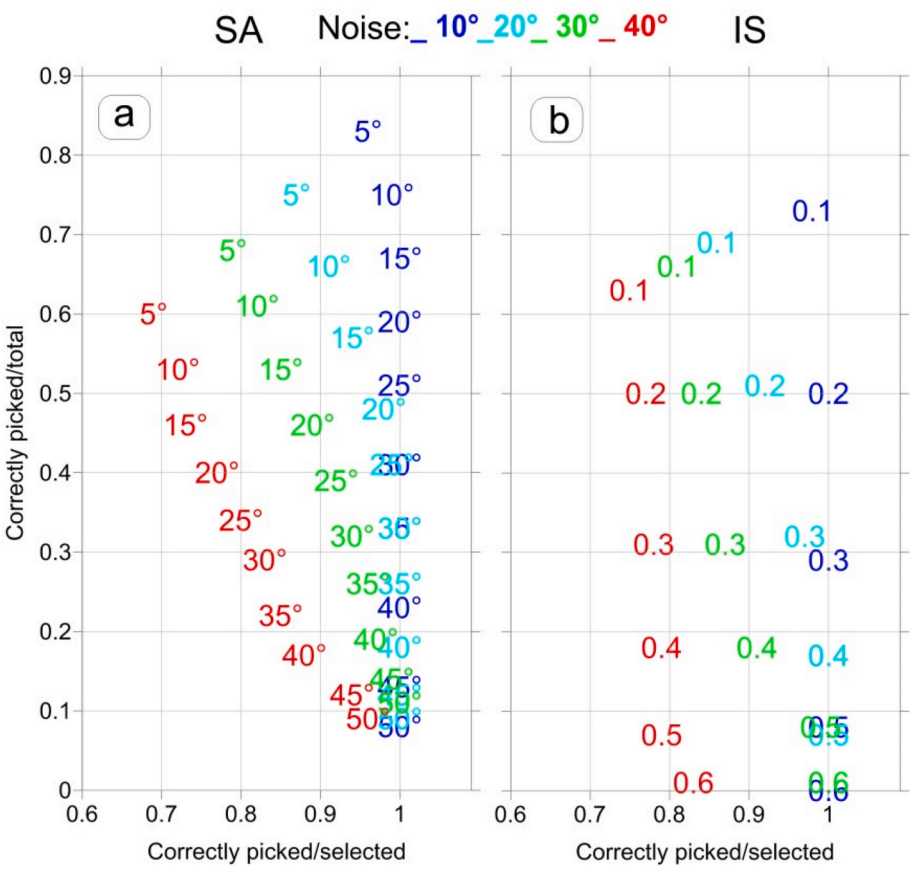

Fig. 8. (a): Minimum misfit difference (dark blue: for a noise level of 10°, light blue: 20°, green: 30°, red: 40°) as a function of correctly picked fault planes with respect to the focal mechanisms that meet the minimum misfit difference (CP/S) (*x*-axis) and with respect to all the focal mechanisms (CP/T) (*y*-axis). (b) Minimum instability coefficient difference for different noise levels corresponding to the same colours as for (a) as a function of CP/S (*x*-axis) and CP/T (*y*-axis). Computations are for reverse stress regime, $\mu = 0.5$ and $R = 0.5$.

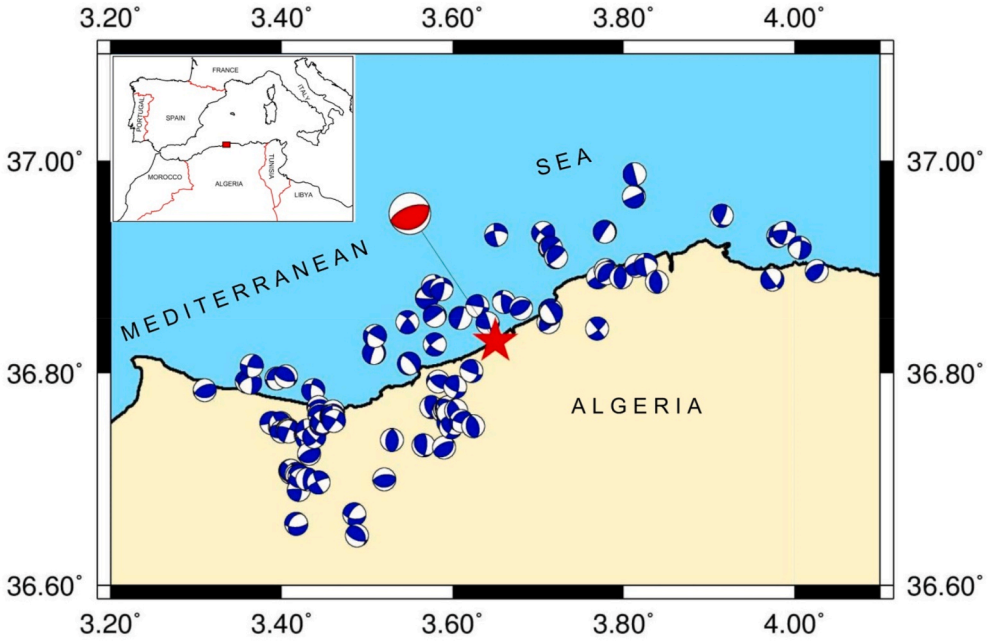

Fig. 9. Focal mechanisms of the aftershocks (blue beach balls) of the Boumerdes earthquake (Mw = 6.8). Red beach ball and red star are the focal mechanism and epicentre of the main shock, respectively. The study area is marked by a red rectangle in the inset.

striking N60° (over 65 km) to N102° (over 13 km) on the western part, as depicted in Fig. 13. This is confirmed by the strike distribution in this area as shown in Fig. 14a where fault planes plunging towards the east and the SE could be associated with the SW part of the fault modelled by Bellabès et al. (2009). Further to the east, on the continent, we can observe through Fig. 14b that aftershocks with fault planes having an azimuth around 45° could be associated with the NE part of the main fault. It is noteworthy that these aftershocks show fault planes whose orientation (Fig. 14b) is mostly in agreement with the main fault geometry. However, the fault plane orientations associated with the

Table 1
Minimum instability difference (min ΔI) as a function of CP/S and CP/T for a noise level of 20° and 40°, shape ratio $R = 0.21$, friction $\mu = 0.55$. Computations have been performed for σ_1, σ_2 and σ_3 principal stress directions (azimuth/plunge) of 142°/18°, 50°/8° and 296°/70°, respectively.

Min ΔI	CP/S (20°)	CP/T (20°)	CP/S (40°)	CP/T (40°)
0.10	0.89	0.76	0.79	0.71
0.20	0.94	0.67	0.81	0.65
0.30	0.98	0.55	0.84	0.59
0.40	1.00	0.41	0.88	0.50
0.50	1.00	0.26	0.91	0.38
0.60	1.00	0.08	0.94	0.20
0.70	1.00	0.01	0.98	0.06
0.80	1.00	0.00	1.00	0.01

aftershocks located offshore (Fig. 14c) present a high diversity, suggesting more complex tectonics, probably related to the transition zone.

It is to be noted that most of the identified fault planes have strikes ranging between 0° and 90°, while those of the corresponding auxiliary planes are from 135° to 270° (Fig. 15), thus confirming a clear discrimination between the two nodal planes and the robustness of the method used for picking faults.

5. Discussion and conclusion

We evaluated the probability of identifying faults for a set of focal mechanisms when applying a uniform stress field. The fault identification enables tectonic interpretations and improves the accuracy of the stress inversion from the focal mechanisms. The presented method was tested on synthetic data and then it was applied to the aftershocks of the May 21st, 2003, Mw6.8 Boumerdes (Algeria) earthquake. We compared two alternative approaches for selecting true fault planes: (1) the fault instability (IS) criterion, and (2) the smallest misfit (SA) criterion. The efficiency and robustness of both approaches were studied using the fraction of correctly picked faults with respect to the set of focal mechanisms (CP/T fraction) and with respect to focal mechanisms that meet the conditions on the misfit (CP/S fraction).

In order to compute the probability of correctly picked faults, we generated focal mechanisms by randomly sampling the strike and dip angles and selecting the fault plane satisfying the Mohr-Coulomb failure condition as suggested by Vavryčuk (2015) and Martínez-Garzón et al. (2016). The true fault planes were noised uniformly with levels up to 45°. In a second stage, we evaluated the probability of correctly picked faults with respect to a given minimum misfit and minimum misfit difference values, as tested by Gephart and Forsyth (1984) and Michael (1987). The results showed that only the minimum misfit difference has an effect on the probability of the fault identification. Similarly, when the instability criterion is used, the maximum value of instability of correctly picked faults does not affect the results and only the minimum instability difference impacts the findings.

Our tests revealed that the IS criterion is more robust than the SA criterion, as highlighted by Martinez-Garzón et al. (2016). Moreover, the IS criterion is even more robust at high noise levels; this is consistent with the results of Lund and Slunga (1999) and Martinez-Garzón et al. (2016). However, when the shape ratio R and the friction coefficient μ are varied, it is clear that the fraction of correctly picked faults is not always higher when using the IS criterion. Indeed, as shown previously, the difference in the computed fractions when using the IS and SA criteria is positive for some values of R and μ, but may be negative for

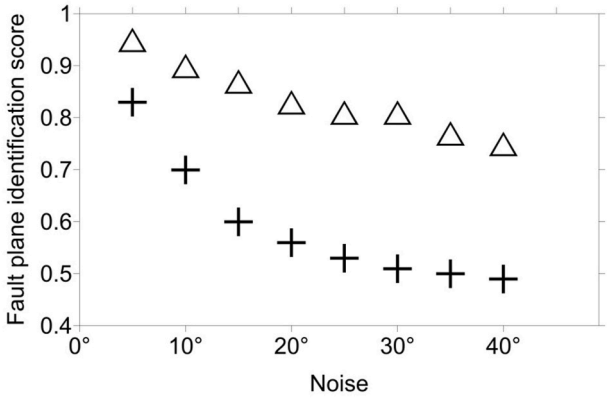

Fig. 11. Fault plane identification score as a function of noise level (5°–40°) for reverse faulting, $R = 0.21$ and coefficient of friction $\mu = 0.55$. Plus signs and triangles relate to the misfit criterion (SA) and the instability criterion (IS), respectively.

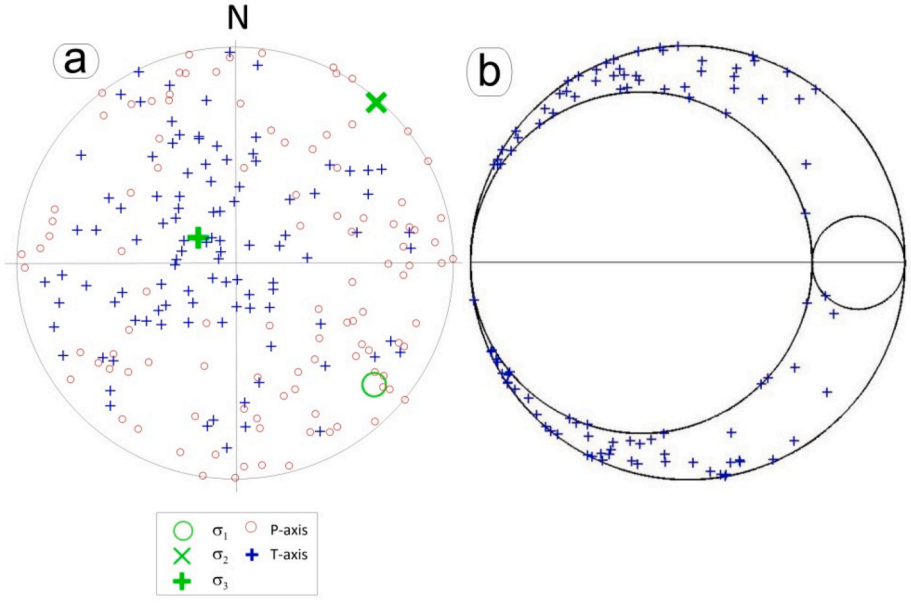

Fig. 10. a) Lower hemisphere projection of the three principal stresses as well as P and T axes of the focal mechanisms. b) Mohr's circle diagram showing the fault planes.

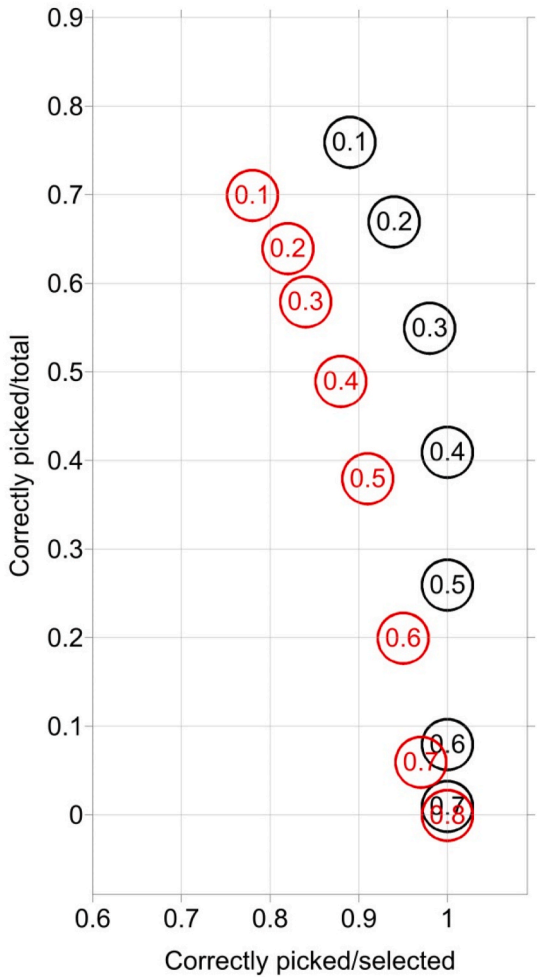

Fig. 12. Minimum instability difference as a function of correctly picked faults with respect to the focal mechanisms that meet the minimum instability difference (CP/S) (*x*-axis) and with respect to all the focal mechanisms (CP/T) (*y*-axis). Black and red circles surrounding the minimum instability difference values are for a noise level of 20° and 40°, respectively.

other values. We may note that the calculations were performed for reverse tectonic regime with noise levels of 10°, 20° 30° and 40°. For each noise level, we can find the R and μ values where the two fractions are equal, allowing us to determine the regions where the IS or SA selection criterion is more robust. It was found that the IS criterion yields higher fractions except for $R > 0.5$ and $\mu < 0.5$. This is consistent with Lund and Slunga (1999) who revealed that the IS criterion could fail for weak faults due to low friction. Knowledge of the efficiency of the two criteria for various combinations of R and μ can thus be used for improving the selection procedure of correct faults when inverting the focal mechanisms for accurate tectonic stress. While Vavryčuk (2014) used the IS method for selecting the correct faults only, we suggest to combine both IS and SA methods similarly as done in Lund and Slunga (1999).

We compared results obtained by forward numerical modelling with those of Martinez-Garzón et al. (2016) who used an inverse method to investigate the fraction of correctly picked fault planes. Whatever the noise level, the fraction of faults identified by the inverse method using the SA criterion is only 50%, whereas the direct problem estimates this probability at more than 70% for a noise level of 40°. We can emphasise the inconsistencies between the two findings. On the other hand, we can point out that the inverse method (Martinez-Garzón et al. 2016), when the IS criterion is used, yields a fraction of correctly picked faults very close for shape ratio R of 0.1, 0.5 and 0.9, whereas the direct method we used clearly shows that this fraction is lower for high values of R and low friction μ. Here again, the two methods do not lead to the same results. These differences highlighted by the two approaches are probably related to the robustness of the inversion method, which would be estimated more efficiently by comparing the results of the inversion method with those given by forward modelling.

The above considerations are supported by Ellsworth and Zhonghuai (1980) who identified fault planes using a combinatorial approach. They proposed inverting each set among all the possible sets of fault plane choices. The set of fault planes and their slip vectors that best fit a single stress tensor is considered to be correct and the corresponding stress tensor the optimum stress solution. However, as the authors pointed out, the number of possible combinations might be quite high as it increase as 2^n, where n is the number of used focal solutions. On the other hand, Lund and Slunga (1999) indicated that if the faults match exactly the stress tensor (SA criterion) and are the most unstable (IS criterion), both fault-picking methods will lead to the correct faults and the correctly retrieved stress tensor. However, the inversion results will be different if

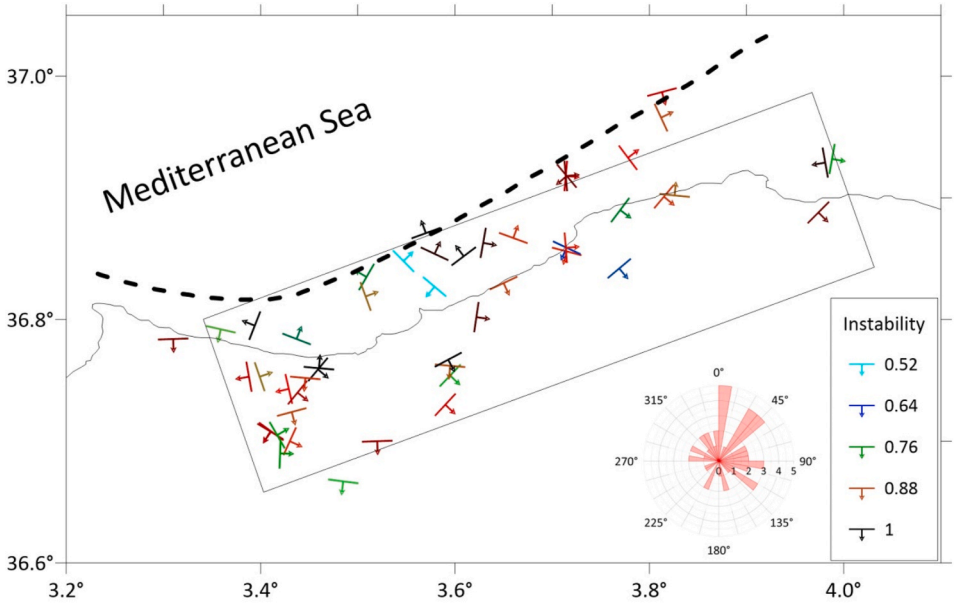

Fig. 13. Orientations and dip directions of the 88% correctly picked faults with their instability coefficient (bottom right inset). Coloured straight lines and arrows indicate the strike and dip direction of the faults, respectively. Rose diagram (inset) describes the fault orientation (strike) pattern. The rectangle represents the main fault of the Boumerdes earthquake as it has been modelled by Delouis et al. (2004). Dashed line marks the fault tip position of the preferred model of Bellabès et al. (2009).

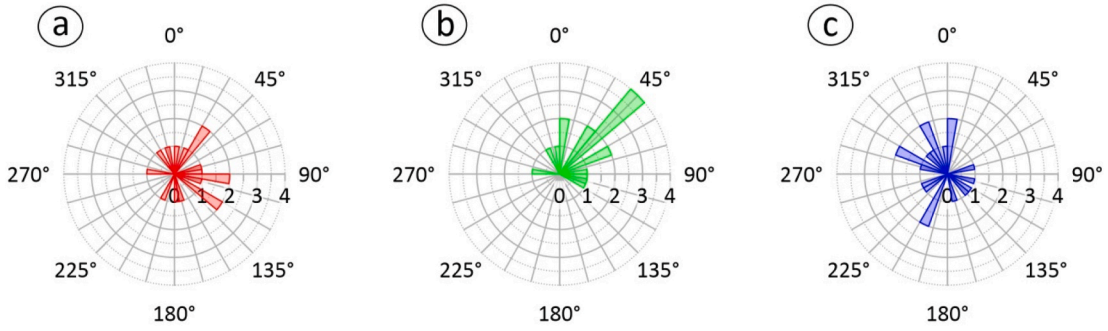

Fig. 14. Rose diagram for strikes of the correctly identified faults for the western cluster (first group) (a), eastern part (second group) (b) and focal mechanisms of the offshore events (third group) (c).

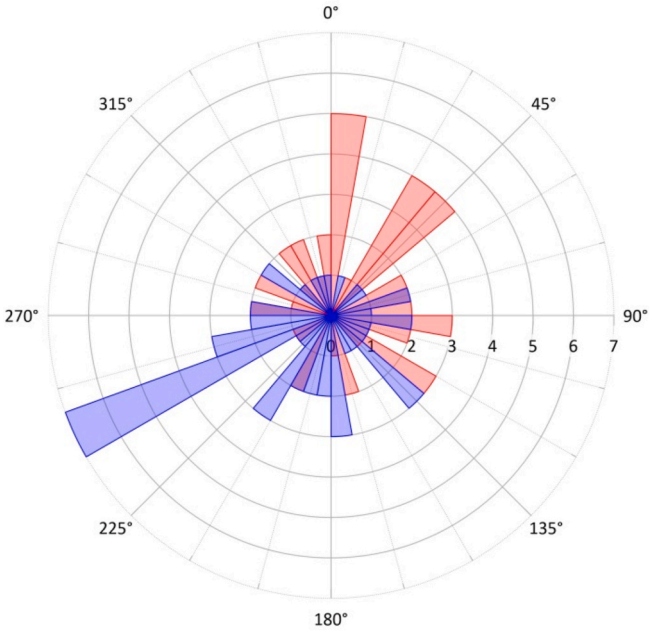

Fig. 15. Rose diagram for strikes of the correctly identified faults (red) and their auxiliary planes (blue).

noise is added to the synthetic data, because both selection methods are differently sensitive to noise.

In the case study, we computed the fractions of correctly picked faults using the highest instability criterion. This concerned 104 focal mechanisms of the aftershocks of the May 21, 2003 Boumerdes (Algeria) earthquake, compiled from Kherroubi et al. (2017) and Ayadi et al. (2008). The faults were determined using the STRESSINVERSE code developed by Vavryčuk (2014). We found that 50 selected nodal planes have 88% probability of being faults. The analysis of the picked faults of the eastern part of the onshore study area confirmed the plunge direction of the main fault which is towards the SE. A correlation is also observed between the aftershocks of the western study area with the N102° oriented fault highlighted by Bellabès et al. (2009). The other focal mechanisms which are those of the aftershocks that occurred offshore show faults striking in various directions, indicating tectonic complexity that would be related to the transition zone.

The results of the inversion code STRESSINVERSE of Vavryčuk (2014) show that when a sufficient level of the probability of peacking correct faults (here, 88%) is chosen, we observe a consistency between the tectonics of the study area and the fault planes that are identified by the code. This also shows that the iterative method using the instability criterion (SI) developed by Vavryčuk (2014) allows a correct identification of faults, as was shown through the application of the STRESSINVERSE code on the slickenside data of the Central Ridge (Central Crete) (Vavryčuk, 2014). Indeed, out of 38 fault planes used, 36 had been identified by the code.

It should be noted that this consistency may be achieved when the minimum misfit criterion (SA) is used, as in the case of the fault analysis of the 2011 Mw7.1 Van earthquake aftershocks (Toker et al., 2017). In the previous study, the faults shown by the high-resolution seismic reflection are consistent with those obtained from the focal mechanisms inversion of the aftershocks. In this case, the inversion code used was that of Gephart (1990) which is based on an iterative process that picks the faults among the two nodal planes, using the slip angle method (SA). The study performed by Toker et al. (2017) showed that the Van region was subject to a reverse faulting stress, with a shape ratio $R = 0.6$. If we analyze these results in the light of our study, we can note from the 'synthetic tests' section that these parameters (reverse fault regime and $R = 0.6$) correspond to high values of the fault plane identification probability, which could explain the success of the 2011 Van earthquake data inversion.

Declaration of competing interest

The authors declare that they have no known competing financial interests or personal relationships that could have appeared to influence the work reported in this paper.

Data availability

No new data were used for the research described in the article.

Acknowledgements

We would like to thank the two anonymous reviewers for their cogent comments that helped improving the paper. We are particularly grateful to the Editor-in-Chief Dr. Mohamed Abdelsalam for his precious assistance and the great efforts he made in reading our article. The research was partially supported by Czech Science Foundation, grant no 22-10747S.

References

Anderson, E.M., 1951. The Dynamics of Faulting and Dyke Formation with Applications to Britain, second ed. Oliver & Boyd, Edinburgh, p. 206.

Angelier, J., 1979. Determination of the mean principal directions of stresses for a given fault population. Tectonophysics 56, T17–T26.

Angelier, J., Tarantola, A., Valette, B., Manoussis, S., 1982. Inversion of field data in fault tectonics to obtain the regional stress — I. Single phase fault populations: a new method of computing the stress tensor. Geophys. J. Int. 69, 607–621. https://doi.org/10.1111/j.1365-246X.1982.tb02766.x.

Angelier, J., 1984. Tectonic analysis of fault slip data sets. J. Geophys. Res. 89, 5835–5848. https://doi.org/10.1029/JB089iB07p05835.

Argus, D.F., Gordon, R.G., Demets, C., Stein, S., 1989. Closure of the Africa– Eurasia–North America plate motion circuit and tectonics of the Gloria fault. J. Geophys. Res. 94 (B5), 5585–5602. https://doi.org/10.1029/JB094iB05p05585.

Armijo, R., Carey, E., Cisternas, A., 1982. The inverse problem in microtectonics and the separation of tectonic phases. Tectonophysics 82, 145–160. https://doi.org/10.1016/0040-1951(82)90092-0.

Arthaud, F., 1969. Méthode de détermination graphique des directions de raccourcissement, d'allongement et intermédiaire d'une population de failles. Bulletin Société Géologique de France S7-XI (5), 729–737. https://doi.org/10.2113/gssgfbull.S7-XI.5.729.

Ayadi, A., Dorbath, C., Ousadou, F., Maouche, S., Chikh, M., Bounif, M.A., Meghraoui, M., 2008. Zemmouri earthquake rupture zone (Mw 6.8, Algeria): aftershocks sequence relocation and 3D velocity model. J. Geophys. Res. 113, B09301 https://doi.org/10.1029/2007JB005257.

Bellabès, S., Wicks, C., Cakir, Z., Meghraoui, M., 2009. Rupture parameters of the 2003 Zemmouri (Mw6.8) Algeria earthquake from joint inversion of interferometric synthetic aperture radar, coastal uplift, and GPS. J. Geophys. Res. 114, B03406 https://doi.org/10.1029/2008JB005912.

Benouar, D., 2004. Materials for the investigation of historical seismicity in Algeria from the records of past earthquakes. Ann. Geophys. 47 (2), 555–560. https://doi.org/10.4401/ag-3321.

Bott, M.H., 1959. The mechanics of oblique slip faulting. Geol. Mag. 96, 109–117. https://doi.org/10.1017/S0016756800059987.

Byerlee, J., 1978. Fiction of rocks. Pure Appl. Geophys. 116, 615–626. https://doi.org/10.1007/BF00876528.

Carey, E., Brunier, B., 1974. Analyse théorique et numérique d'un modèle mécanique élémentaire appliqué à l'étude d'une population de failles. *C. R. Acad. Sci.* D 279, 891–894.

Carey, E., 1976. *Analyse numérique d'un module mécanique élémentaire appliquée à l'étude d'une population de failles: Calcul d'un tenseur moyen des contraintes à partit des stries de glissement*, PhD thesis. Université Paris Sud.

Delouis, B., Vallée, M., Meghraoui, M., Calais, E., Maouche, S., Lammali, K., Mahsas, A., Briole, P., Benhamouda, F., Yelles, K., 2004. Slip distribution of the 2003 Boumerdes- Zemmouri earthquake, Algeria, from teleseismic, GPS, and coastal uplift data. Geophys. Res. Lett. 31, L18607 https://doi.org/10.1029/2004GL020687.

Ellsworth, W.L., Zhonghuai, X., 1980. Determination of the stress tensor from focal mechanism data (abstract). Eos Trans 61, 1117.

Gephart, J.W., Forsyth, D.W., 1984. An improved method for determining the regional stress tensor using earthquake focal mechanism data: application to the San Fernando Earthquake Sequence. J. Geophys. Res. 89, 9305–9320. https://doi.org/10.1029/JB089iB11p09305.

Gephart, J.W., 1990. FMSI: a Fortran program for inverting fault/slickenside and earthquake focal mechanism data to obtain the regional stress tensor. Comput. Geosci. 16 (7), 953–989. https://doi.org/10.1016/0098-3004(90)90105-3.

Hamdache, M., Pelaez, J.A., Talbi, A., Lopez-Casado, C., 2010. A unified catalog of main earthquakes for northern Algeria from A.D. 856 to 2008. Seismol Res. Lett. 81 (5), 732–739. https://doi.org/10.1785/gssrl.81.5.732.

Jaeger, J.C., Cook, N.G.W., Zimmerman, R.W., 2007. Fundamentals of Rock Mechanics, fourth ed. Blackwell Publishing, p. 488.

Kherroubi, A., Yelles-Chaouche, A.K., Koulakov, I., Deverchere, J., Beldjoudi, H., Haned, A., Semmane, F., Aidi, C., 2017. Full aftershock sequence of the mw 6.9 2003 Boumerdes earthquake Algeria: space-time distribution, local tomography and seismotectonic implications. Pure Appl. Geophys. 174, 2495–2521. https://doi.org/10.1007/s00024-017-1571-5.

Lund, B., Slunga, R., 1999. Stress tensor inversion using detailed microearthquake information and stability constraints: application to Ölfus in southwest Iceland. J. Geophys. Res. 104, 14,947–14,964. https://doi.org/10.1029/1999JB900111.

Martínez-Garzón, P., Ben-Zion, Y., Abolfathian, N., Kwiatek, G., Bohnhoff, M., 2016. A refined methodology for stress inversions of earthquake focal mechanisms. J. Geophys. Res. Solid Earth 121, 8666–8687. https://doi.org/10.1002/2016JB013493.

Meghraoui, M., Maouche, S., Chemaa, B., Cakir, Z., Aoudia, A., Harbi, A., Alasset, P.J., Ayadi, A., Bouhadad, Y., Benhamouda, F., 2004. Coastal uplift and thrust faulting associated with the Mw = 6.8 Zemmouri (Algeria) earthquake of 21 May 2003. Geophys. Res. Lett. 31, L19605 https://doi.org/10.1029/2004GL020466.

Michael, A.J., 1984. Determination of stress from slip data: faults and folds. J. Geophys. Res. 89 (B13), 11517–11526. https://doi.org/10.1029/JB089iB13p11517.

Michael, A.J., 1987. Use of focal mechanisms to determine stress: a control study. J. Geophys. Res. 92, 357–368. https://doi.org/10.1029/JB092iB01p00357.

Nocquet, J.M., Calais, E., 2004. Geodetic measurements of crustal deformation in the western Mediterranean and Europe. Pure Appl. Geophys. 161, 661–681. https://doi.org/10.1007/s00024-003-2468-z.

Pelaez-Montilla, J.A., Hamdache, M., Casado, C.L., 2003. Seismic hazard in Northern Algeria using spatially smoothed seismicity, results for peak ground acceleration. Tectonophysics 372, 105–111. https://doi.org/10.1016/S0040-1951(03)00234-8.

Rothé, J.P., 1950. Les séismes de Kherrata et la séismicité de l'Algérie, vol. 24. Bulletin du Service de la Carte Géologique de l'Algérie, p. 40.

Toker, M., Pınar, A., Tur, H., 2017. Source mechanisms and faulting analysis of the aftershocks in the Lake Erçek area (Eastern Anatolia, Turkey) during the 2011 Van event (Mw 7.1): implications for the regional stress field and ongoing deformation processes. J. Asian Earth Sci. 150, 73–86. https://doi.org/10.1016/j.jseaes.2017.09.017.

Vavryčuk, V., 2011. Principal earthquakes: theory and observations from the 2008 west bohemia swarm. Earth Planet Sci. Lett. 305, 290–296. https://doi.org/10.1016/j.epsl.2011.03.002.

Vavryčuk, V., Bouchaala, F., Fischer, T., 2013. High-resolution fault image from accurate locations and focal mechanisms of the 2008 swarm earthquakes in West Bohemia, Czech Republic. Tectonophysics 590, 189–195. https://doi.org/10.1016/j.tecto.2013.01.025.

Vavryčuk, V., 2014. Iterative joint inversion for stress and fault orientations from focal mechanisms. Geophys. J. Int. 199 (1), 69–77. https://doi.org/10.1093/gji/ggu224.

Vavryčuk, V., 2015. Earthquake mechanisms and stress field. In: Beer, M., et al. (Eds.), Encyclopedia of Earthquake Engineering. Springer, Berlin Heidelberg, pp. 728–746.

Wallace, R.E., 1951. Geometry of shearing stress and relation to faulting. J. Geol. 59, 118–130. https://doi.org/10.1086/625831.

Yelles, K., Lammali, K., Mahsas, A., Calais, E., Briole, P., 2004. Coseismic deformation of the may 21st, 2003, mw = 6.8 Boumerdes earthquake, Algeria, from GPS measurements. Geophys. Res. Lett. 31, L13610 https://doi.org/10.1029/2004GL019884.